Quantifying Rate- and Temperature-Dependent Molecular Damage in Elastomer Fracture

Juliette Slootman,[1] Victoria Waltz,[1] C. Joshua Yeh[1], Christoph Baumann,[2,3]
Robert Göstl[2], Jean Comtet,[1,*] and Costantino Creton[1,†]

[1]*Laboratory of Soft Matter Science and Engineering, ESPCI Paris, PSL University,*
CNRS, Sorbonne Université, 75005 Paris, France
[2]*DWI-Leibniz Institute for Interactive Materials, Forckenbeckstrasse 50, 52056 Aachen, Germany*
[3]*Institute of Technical and Macromolecular Chemistry, RWTH Aachen University,*
Worringerweg 1, 52074 Aachen, Germany

Elastomers are highly valued soft materials finding many applications in the engineering and biomedical fields for their ability to stretch reversibly to large deformations. Yet their maximum extensibility is limited by the occurrence of fracture, which is currently still poorly understood. Because of a lack of experimental evidence, current physical models of elastomer fracture describe the rate and temperature dependence of the fracture energy as being solely due to viscoelastic friction, with chemical bond scission at the crack tip assumed to remain constant. Here, by coupling new fluorogenic mechanochemistry with quantitative confocal microscopy mapping, we are able to quantitatively detect, with high spatial resolution and sensitivity, the scission of covalent bonds as ordinary elastomers fracture at different strain rates and temperatures. Our measurements reveal that, in simple networks, bond scission, far from being restricted to a constant level near the crack plane, can both be delocalized over up to hundreds of micrometers and increase by a factor of 100, depending on the temperature and stretch rate. These observations, permitted by the high fluorescence and stability of the mechanophore, point to an intricate coupling between strain-rate-dependent viscous dissipation and strain-dependent irreversible network scission. These findings paint an entirely novel picture of fracture in soft materials, where energy dissipated by covalent bond scission accounts for a much larger fraction of the total fracture energy than previously believed. Our results pioneer the sensitive, quantitative, and spatially resolved detection of bond scission to assess material damage in a variety of soft materials and their applications.

Subject Areas: Soft Matter

I. INTRODUCTION

Many new soft but tough rubbery materials have been recently discovered [1–4], and new applications such as flexible prosthetics [5], stretchable electrodes [6], or soft robotics [7] continuously emerge. Yet, a credible multiscale quantitative picture of damage and fracture of these materials has still not emerged, in particular, due to our fundamental inability to disentangle the irreversible scission of chemical bonds along the fracture path from dissipation by internal molecular friction [8].

The failure and fracture of soft materials is indeed an inherently multiscale process: The propagation of a macroscopic crack in the material couples molecular covalent bond scission processes at the crack tip, with deformation and energy dissipation in the bulk [9,10]. Elastomers, a representative class of soft materials, are networks of connected flexible polymer chains, which do not display a well-defined localized yielding behavior, such as metals, ceramics, or polymer glasses. When a crack propagates in an elastomer, it is thus impossible to detect when and where bonds break with conventional methods, and the "process zone" (the mechanically damaged region) is treated for lack of information as an energy sink [11–13] or a cohesive zone of zero thickness [14,15].

Within the field of mechanochemistry, synthetic chemists have recently developed new molecules that can respond optically to forces and bond scission processes when suitably incorporated in polymer networks [16–18]. These mechanosensitive molecules have been incorporated into multiple network elastomers and in filled elastomers and have given important new insights into sacrificial bond scission during the fracture process [19–21]. However, the dioxetane-based mechanophore previously used by Ducrot *et al.* emits light only upon bond scission, cannot be

calibrated easily to compare different materials in absolute terms, and gives a very low signal (approximately one emitted photon every 1000 broken bonds). As a result, the first generation of mechanophores could detect bond scission only in reinforced elastomers containing sacrificial bonds in the bulk by design, and quantitative comparisons between different materials were not possible. Furthermore, the low sensitivity and real time emission upon crack propagation made it challenging to address dynamic problems like crack propagation at different rates with a high spatial resolution. No signal was detected, for example, upon fracture of simple unfilled elastomers [19], making it impossible to address the questions of the current paper. It should be noted also that, while the importance of breaking covalent sacrificial bonds to toughen soft materials, and elastomers, in particular, has been amply demonstrated in several materials [19,20,22], the strain rate and/or temperature dependence of bond breakage of covalent (not dynamic) bonds has never been addressed. Yet this rate and T dependence of the fracture energy in elastomers has major technological consequences in applications [8] and is a long-standing and still open scientific question [8,9,12].

Recently, Göstl, Sijbesma, and co-workers reported a new fluorogenic mechanophore based on a Diels-Alder (DA) adduct of π-extended anthracene [18,23] that fluoresces stably and sensitively upon force-induced bond scission, making it an ideal candidate for quantitative studies on simple elastomers. This high sensitivity and stability make it possible to label simple networks of classical unfilled elastomers, which are at the heart of all molecular fracture theories.

We incorporate this mechanophore as a chain scission-reporting cross-linker into a series of acrylate elastomers prepared by photoinitiated free radical polymerization (Tables I and II and Appendix A). By fracturing these labeled elastomers at different temperatures and strain rates and performing *postmortem* fluorescence imaging, we could improve sensitivity by at least 2 orders of magnitude with respect to our previous strategy [19] and obtain unprecedented spatially resolved quantitative insight into the coupling between molecular bond scission processes at the crack tip and bulk viscoelastic dissipation in these soft materials.

II. FRACTURE PROPAGATION IN ELASTOMERS

We propagate cracks by stretching single-edged notched samples of elastomeric networks in uniaxial extension at different stretch rates $\dot{\lambda}$ and temperatures T [Fig. 1(a) and Appendix B]. The networks are synthesized from ethyl acrylate (EA) or methyl acrylate (MA) monomers and 1,4-butanediol diacrylate (BDA) as nonmechanoresponsive cross-linker and are labeled with additional 0.02 mol% (relative to monomer) of the mechanophore diacrylate cross-linker (see Tables I and II and synthesis details in Appendix A and in Supplemental Material [24]). The total cross-link density is of the order of $\nu_x \sim 10^{25}$ m^{-3}. These mechanical measurements [Fig. 1(b)] are used to extract the macroscopic fracture energy Γ_c [J · m^{-2}] (energy necessary to propagate a unit area of crack), using a fracture mechanics method [25], as well as the crack propagation speed v_{crack} (see Appendix B). For the poly(methyl acrylate) elastomer (PMA-DA-0.4, see Table I), we observe a decrease in fracture energy for an increasing temperature and for decreasing crack propagation speed v_{crack} (obtained by varying the stretch rate) (Fig. S5 in Supplemental Material [24]), a typical observation in elastomers [26].

As shown in Fig. 1(c), following classical time-temperature superposition of the data [12], this macroscopic fracture energy obtained for various temperatures (square) and stretch rates (circles) can be plotted as a sole function of a reduced crack speed $a_T \cdot v_{\text{crack}}$. The factor a_T is a decreasing function of the temperature, characterizing viscoelastic dissipation in the sample, and is measured from linear rheology (reported in Fig. S7 in Supplemental Material [24]). This overall rescaling leads to a power-law increase in the fracture energy with crack propagation speed [dashed line, Fig. 1(c)], characterizing the importance of viscoelastic processes during fracture propagation.

For a lack of molecular insights on the actual dissipative processes occurring at the crack tip, this rate-dependent behavior has always been described by the phenomenological expression $\Gamma_c = \Gamma_0 \cdot [1 + f(a_T . v_{\text{crack}})]$, decoupling the rate-independent bond scission processes in the network Γ_0, occurring strictly in the fracture plane [27], from bulk rate-dependent viscoelastic dissipation [characterized by the function $f(a_T . v_{\text{crack}})$ with $f(v \to 0) = 0$], predicted

TABLE I. Sample and material parameters. PMA-DA-0.4, PMA-DA-0.2, and PEA-DA-0.5 are synthesized with 0.02 mol% of DA mechanophore and, respectively, 0.43, 0.22, and 0.5 mol% of total cross-linker. See Appendix A for details on material synthesis. The cross-link density ν_x is extracted from fits of the stress-strain curve (see Appendix B).

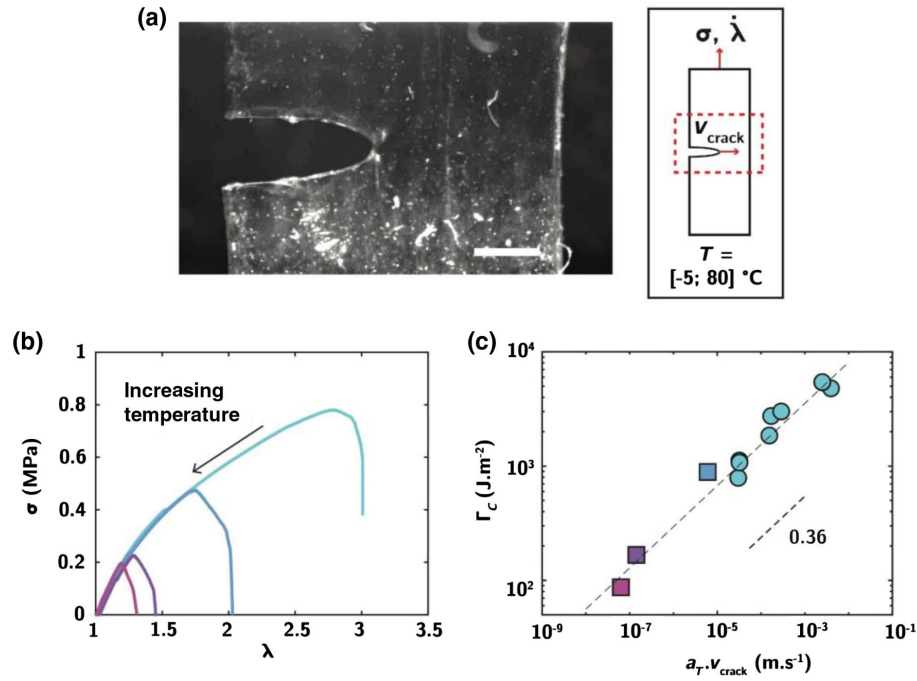|	Modulus E	Glass transition temperature T_g	Cross-link density ν_x	C—C bonds per strand N_x	Strand areal density Σ_{LT}
PMA-DA-0.4	1.15 MPa	18 °C	4.6×10^{25} m^{-3}	370	1.9×10^{17} m^{-2}
PMA-DA-0.2	1 MPa	18 °C	2.8×10^{25} m^{-3}	620	1.5×10^{17} m^{-2}
PEA-DA-0.5	1 MPa	−18 °C	4.2×10^{25} m^{-3}	400	1.8×10^{17} m^{-2}

FIG. 1.   Macroscopic fracture propagation in elastomers. (a) Image of a notched sample during a fracture test. The scale bar is 1 mm. Inset: Geometry of the fracture test, with a notched sample in uniaxial extension submitted with a constant stretch rate $\dot{\lambda}$ to an increasing stress σ until a crack propagates at speed v_{crack}. (b) Stress-strain curves for notched PMA-DA-0.4 elastomer samples at temperature $T = 25, 40, 60,$ and $80\,°C$ (from light blue to purple). (c) Variation of the fracture energy Γ_c as a function of rescaled crack velocity $a_T.v_{crack}$. Squares correspond to samples fractured at different temperatures and constant stretch rate $\dot{\lambda} = 3 \times 10^{-3}$ s^{-1} and circles to samples fractured at 25 °C and varying stretch rates $\dot{\lambda} = [3 \times 10^{-4}; 3 \times 10^{-3}; 3 \times 10^{-2}]$ s^{-1}.

from the linear viscoelastic properties of the material [11,28,29] or simply correlated with mechanical hysteresis [30]. This picture is clearly oversimplified: Assuming Γ_0 to be velocity independent is in contradiction with the general expectation for rate-dependent materials [31], and quantitative agreement with data if a constant Γ_0 is assumed requires the introduction of arbitrary length or energy scales [8,32] or predicts viscoelastic dissipation to take place down to typically unphysically small molecular distances at the crack tip [12]. Here, we tackle the inconsistencies in the current models by quantifying for the first time molecular bond breakage at the crack tip during fracture propagation in these materials.

III. MECHANOPHORES QUANTITATIVELY REPORT STRAND SCISSION

As shown in Fig. 2, by incorporating DA adduct mechanophores as cross-linkers in the network, we can quantify chain scission during elastomer failure [Fig. 2(a); typically, 5%–10% of overall cross-links are mechanophores]. In its native form, the mechanophore is nonfluorescent [Fig. 2(b)(i)]. If a sufficient force is applied to the bond, it can undergo cycloelimination (a retro DA reaction), which is irreversible at low temperature [18], leading to the release of a fluorescent π-extended anthracene moiety [Fig. 2(b)(ii), orange molecule]. As previously
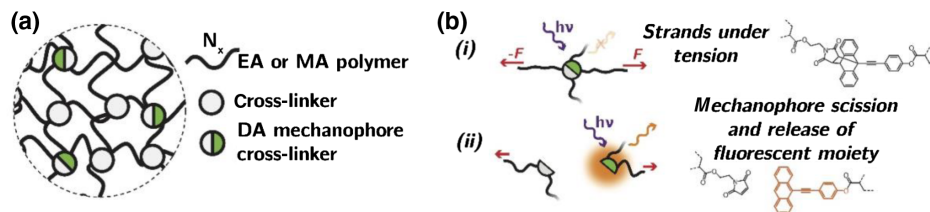

FIG. 2.   Strategy for mechanophore incorporation and quantification of the activation. (a) Incorporation of mechanophores at cross-link points in the elastomer network. (b) Mechanophore activation reports for strand scission. (i) Nonfluorescent form of the DA mechanophore, connected to a strand under tension. (ii) Irreversible scission of the mechanophore (retro DA reaction), leading to the release of a fluorescent anthracene moiety, reporting for strand breakage (orange). Dashed bonds show connectivity to the network.

reported [33,34], the retro DA reaction is greatly accelerated under force with a significantly higher mechanochemical scission rate compared to homolytic C—C bond scission. When connected to the mechanophore, a stressed polymer strand under extension, thus, fails more likely through scission of this mechanochemically weaker bond [Fig. 2(b)(ii)], leading to the activation of fluorescence.

Since the mechanophore bond is weaker than the C—C bond, an important question is its ability to quantitatively and reliably report for strand breakage. The key aspect to understand here is that, in a 3D network of entangled and cross-linked polymer chains, the forces on bonds along the chain and at cross-link points are not homogeneous, since the strands between cross-links have a distribution of lengths (number of monomers) and conformations (some are more coiled than others). In elastomers, cross-link points deform affinely with macroscopic deformation. In a mean-field representation neglecting interactions between strands, only the strands that are close to their maximum extension see forces of the order of the scission force as discussed in detail by Vernerey *et al.* [35].

Of course, the breakage force of a strand containing a mechanophore will be lower than that of a C—C bond. However, because of the strong nonlinearity of the force-extension curve of the strands [35,36], a C—C bond would have broken anyway at only a slightly larger macroscopic extension than the mechanophore. As a result, the fluorescence should, in principle, report broken strands quantitatively but simply at a slightly lower value of stretch than what C—C bonds would break at. In this work, we hypothesize that the fraction ϕ of cleaved chains in the overall material, a characteristic of local damage of the network, is equal to the fraction of cleaved mechanophores. To validate this important hypothesis, we verify that the number of activated mechanophores during mechanical testing varies indeed linearly with the initial fraction of DA adduct used as cross-linker (Fig. 8 in Appendix C) and that the mechanophore-labeled networks have nearly identical mechanical properties as the pristine ones within the reproducibility of the experiment (Fig. S6 in Supplemental Material [24]). We add a simple quantitative argument rationalizing this result in Appendix C.

The extent of strand failure and damage in the material can now be quantified postmortem by measuring the activation of fluorescent mechanophores following crack propagation in various conditions. We use confocal mapping to quantify strand scission in the material normal to the crack surface through the measurement of the local fluorescence intensity due to mechanophore activation [Fig. 3(b)]. Confocal mapping reduces out-of-focus light and allows the measurement of intensity in local volumes $x \times z \times y$ ("voxels") of typically $1.8 \times 1.8 \times 12 \ \mu\mathrm{m}^3$ inside of the material (see Appendix C).

Figure 3(a) shows $500 \times 500 \ \mu\mathrm{m}^2$ maps of the fluorescence intensity in planes normal to the crack surface, in two

PMA-DA-0.4 samples fractured at stretch rates $\dot{\lambda} = 3.10^{-3} \ \mathrm{s}^{-1}$ and temperature (i) $T = 80\,^\circ\mathrm{C}$ and (ii) $T = 25\,^\circ\mathrm{C}$, conditions where (i) low and (ii) high bulk viscoelastic dissipation is active [Fig. S7(d) [24]]. We observe in these 2D maps a maximum in fluorescence intensity at the crack surface and an intensity profile relatively invariant along the directions of crack propagation [vertical x direction in Fig. 3(a)]. Remarkably, large differences in the fluorescence profile are observed when comparing these two fracture conditions. For the first sample, fractured at $T = 80\,^\circ\mathrm{C}$, bulk viscoelastic dissipation is low, and fluorescence activation (and, hence, network scission) is spatially confined to a region a few micrometers wide at the crack surface. When the sample is fractured at $T = 25\,^\circ\mathrm{C}$, where bulk viscoelastic dissipation is much higher, we observe both an increase in intensity, revealing a larger local density of broken bonds, as well as a much larger spatial extension of the damage, with strand scission progressively decreasing toward the bulk of the material over a hundred micrometers. As similar damage maps are observed along the sample thickness [z direction, Fig. 3(b)], we restrict all further quantitative analysis to a constant depth of $100 \ \mu\mathrm{m}$ in our samples (see Appendix C). Note that a significant thermal contribution to the retro DA fluorescence activation can be ruled out, as it would lead to increasing fluorescence with increasing temperature (Appendix C).

For quantification, the local fluorescence intensity is then compared to calibration samples with known amounts of 9-((4-anisyl)ethynyl)anthracene reference fluorophore [18] [equivalent to the activated anthracene, Fig. 2(b)(ii)] (Appendix C). As shown in Fig. 3(c), we extract from these raw confocal images the spatial profile of the fraction ϕ of activated mechanophores, equivalent to the fraction of broken strands [Fig. 3(c), averaged spatial profile shown, respectively, in red (i) and blue (ii)]. As already shown in Fig. 3(a), the damage profile varies strongly with the fracture temperature. We define a damage length L, characterizing the spatial extension of strand scission in the material down to the detection threshold concentration of $(4 \times 10^{-3})\%$ and equal, respectively, to $L_{(\mathrm{i})} = 25 \ \mu\mathrm{m}$ and $L_{(\mathrm{ii})} = 250 \ \mu\mathrm{m}$ at $80\,^\circ\mathrm{C}$ and $25\,^\circ\mathrm{C}$, respectively [Fig. 3(c), inset]. For sample (ii), the fraction of broken bonds ϕ in the bulk material, at $50 \ \mu\mathrm{m}$ from the crack surface, is of the order of 0.1%, corresponding to 10^{22}–10^{23} broken strands per m^3 (one strand every approximately 20–40 nm). As shown in the inset, this damage profile $\phi(z)$ decays here approximately exponentially in the bulk of the material.

To quantify further the extent of damage in the network in each condition, we compute the density Σ of cleaved strands per unit area of crack surface created. This quantity $\Sigma = 2\nu_x \int \phi(z)dz$ (with ν_x the volume density of cross-links) is obtained by integrating the damage $\phi(z)$ normal to
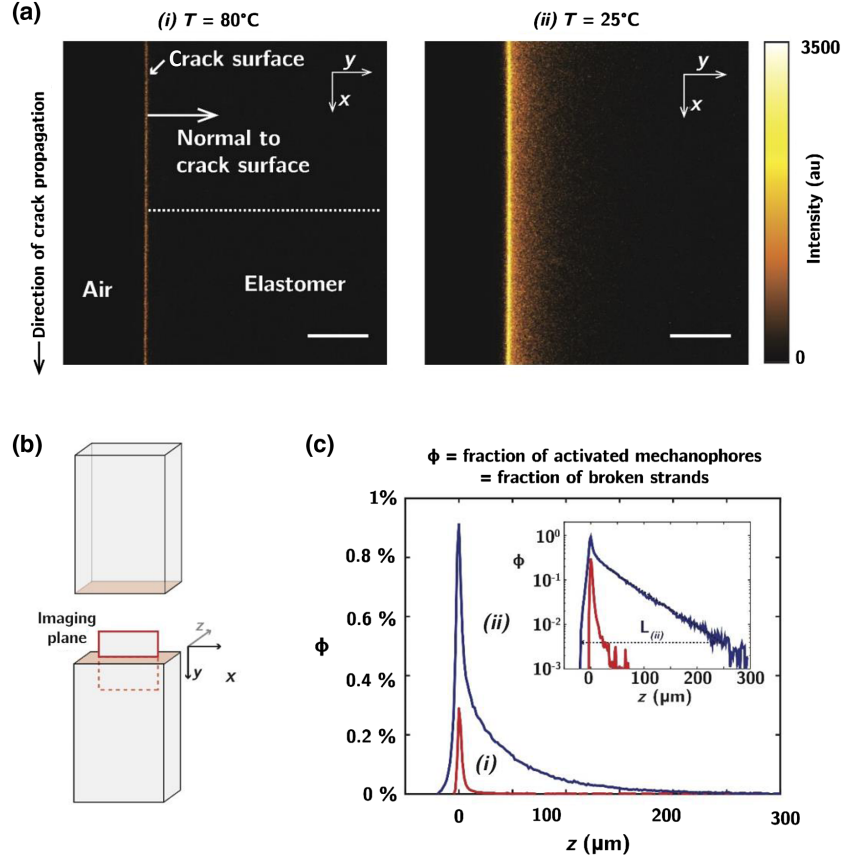
FIG. 3. Postmortem damage quantification through confocal imaging. (a) Postmortem image of fluorescence activation in a poly (methyl acrylate) sample (PMA-DA-0.4, Table I) measured by confocal fluorescence microscopy. Samples are fractured at $\dot{\lambda} = 3 \times 10^{-3}$ s^{-1}, respectively, in conditions of (i) low and (ii) high viscoelasticity, at (i) $T = 80\,°C$ and (ii) $T = 25\,°C$. Pixel size is 1.63 μm. The scale bar is 100 μm. The direction of crack propagation is along the x direction (vertical). (b) Schematic of the confocal imaging plane (in red), perpendicular to the crack surface (shown in orange). The direction of crack propagation is along the x direction, the stretch direction along y, and sample thickness along z. (c) Average spatial damage profile ϕ for conditions (i) and (ii), with damage ϕ defined as the fraction of broken strands in the material, equal to the fraction of activated mechanophores. The inset shows the profiles in lin-log scale, with $L_{(ii)}$ characterizing the spatial extension of damage for condition (ii).

the crack surface and is found to be, respectively, $\Sigma_{(i)} \approx 1.2 \times 10^{18}$ m^{-2} and $\Sigma_{(ii)} = 2.2 \times 10^{19}$ m^{-2} for, respectively, 80 °C and 25 °C. The factor 2 in the expression of Σ accounts for the fact that each crack surface includes only half of the total damage per unit area. Σ can be conveniently normalized by Σ_{LT}, the *minimum* number of strands that need to be broken for a crack to propagate in the material [27]. Σ_{LT} can be estimated as $1/2 \times v_x \langle R_0^2 \rangle^{1/2}$, with v_x the volume density of cross-linking points and $\langle R_0^2 \rangle^{1/2}$ the average distance between cross-links. Following Gaussian statistics, Σ_{LT} can be expressed as a function of material parameters [37] (Appendix C) and is found to be of the order of 10^{17} strands per m^{-2} (Table I). For the two conditions in Fig. 3, we find, respectively, $\Sigma_{(i)}/\Sigma_{LT} \approx 6$ and $\Sigma_{(ii)}/\Sigma_{LT} \approx 110$, a very large value demonstrating that, in this condition, crack propagation in the material involves the failure of many more bonds than a single molecular plane and extends over distances in the material that are

more than 4 orders of magnitude larger than the network mesh size.

IV. VISCOELASTIC DISSIPATION AND CHAIN DAMAGE

The strong coupling between damage and viscoelastic dissipation in the sample uncovered in Fig. 3 and the large amount of molecular damage following crack propagation is an unexpected and novel result, never incorporated in any fracture model for lack of experimental insight. Using the same quantification technique, we carry out coupled mechanical measurements and postmortem damage mapping and quantification, systematically varying the stretch rates and temperature during fracture propagation. In order to increase the range of probed viscoelastic dissipation regimes, we furthermore compare the two PMA and PEA networks of respective glass transition $T_g^{MA} = 18\,°C$ and $T_g^{EA} = -18\,°C$ but similar cross-link density (Table I).
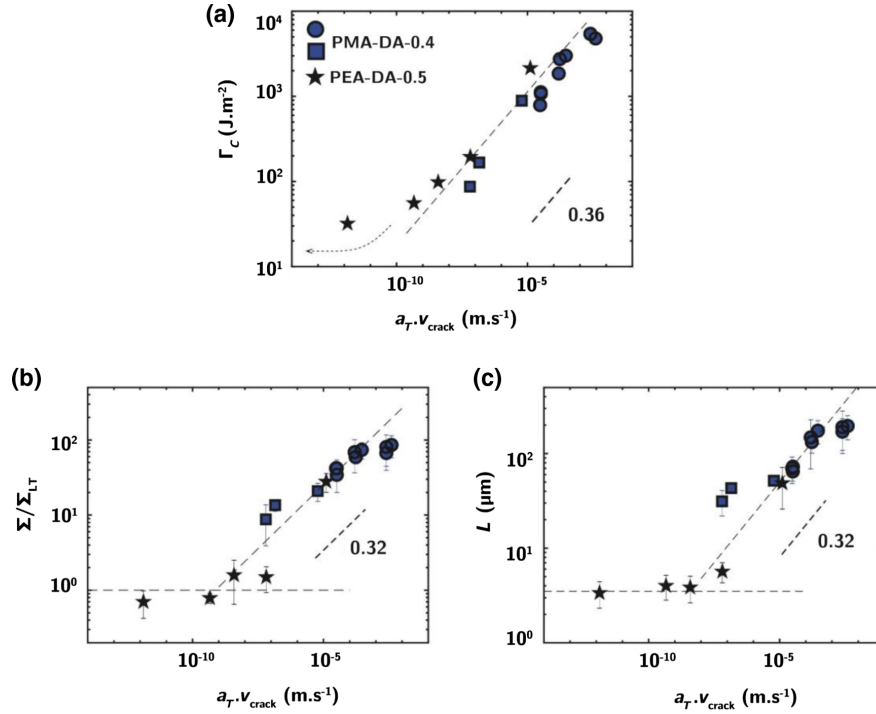
FIG. 4. Coupling of damage with viscoelastic dissipation in the material. (a) Fracture energy Γ_c as a function of rescaled crack velocity $a_T \cdot v_{\text{crack}}$, for the PMA-DA-0.4 (blue squares and circles) and PEA-DA-0.5 samples (black stars). The reference temperature is taken at 25 °C for the PMA sample (see Fig. S7 [24]). At a low rescaled crack speed, Γ_c becomes less dependent on crack speed for PEA. The blue square corresponds to samples fractured at stretch rate $\dot{\lambda} = 3 \times 10^{-3}$ s^{-1} and different temperature and blue circles to samples fractured at 25 °C and stretch rates $\dot{\lambda} = [3 \times 10^{-4}; 3 \times 10^{-3}; 3 \times 10^{-2}]$ s^{-1}. (b) Normalized areal density of broken strands as a function of the rescaled crack velocity. The horizontal line corresponds to the Lake-Thomas prediction $\Sigma/\Sigma_{\text{LT}} = 1$. (c) Damage length L as a function of the rescaled crack velocity. Error bars in (b) and (c) show the standard deviation based on four local confocal measurements on each fractured sample.

Rescaling between the EA and MA data is obtained by adjusting the viscoelastic shift factor $a(T)$ based on the onset of the glass transition in the storage modulus (Fig. S7 [24]). As shown in Fig. 4(a), we observe for these two materials a power-law increase in the fracture energy with crack propagation speed [dashed lines, Fig. 4(a)]. Because of the low glass transition temperature of the PEA network, we reach for this sample a low-velocity regime for which Γ_c becomes less dependent on the crack speed, here for $a_T \cdot v_{\text{crack}} < 10^{-10}$ m·s^{-1} [Fig. 4(a), dashed arrow]. As discussed above, this overall rescaling of Γ_c with reduced crack speed $a_T \cdot v_{\text{crack}}$ has been classically accounted for by spatially decoupling rate-independent processes at the crack tip with bulk viscoelastic dissipation.

Our methodology developed in Figs. 2 and 3 allows us to revisit this oversimplified picture, as we can now quantify for each of these experimental conditions the density of strands broken per unit area of crack. To compare the two materials, we plot the normalized damage $\Sigma/\Sigma_{\text{LT}}$ as a function of $a_T \cdot v_{\text{crack}}$. As shown in Fig. 4(b), this normalized areal density of broken strands shows a similar trend as that of the fracture energy Γ_c, with a power-law increase in the density of broken bonds with increasing reduced crack

velocity [dashed line in Fig. 4(b)]. This significant increase in covalent bond scission with crack speed contradicts the classical picture of fracture propagation, which assumes strand breakage to be independent or weakly dependent on crack velocity [11,27,38]. At very low crack velocities, we do recover a limiting behavior for which damage appears (within our experimental spatial resolution) indeed solely confined to a molecular plane, as characterized by $\Sigma/\Sigma_{\text{LT}} \approx 1$ [Fig. 4(b), horizontal dashed line]. We also observe a saturation in damage due to bond scission for the PMA sample in the limit of high crack velocities ($a_T \cdot v_{\text{crack}} > 10^{-3}$ m·s^{-1}). Finally, as shown in Fig. 4(c), the damage length L characterizing the extension of damage in the material shows a similar trend as the normalized bond breakage $\Sigma/\Sigma_{\text{LT}}$. Viscoelasticity, strand failure, and fracture energy appear here strongly coupled.

We rationalize this coupling between viscoelastic dissipation and bond scission in the network as due to an increase of the elastoadhesive length scale [9] at propagation Γ_c/E with increasing reduced crack velocity. In viscoelastic materials, propagating the crack at a faster speed leads to more dissipation (the dissipative modulus E'' increases with the strain rate) and requires higher values of
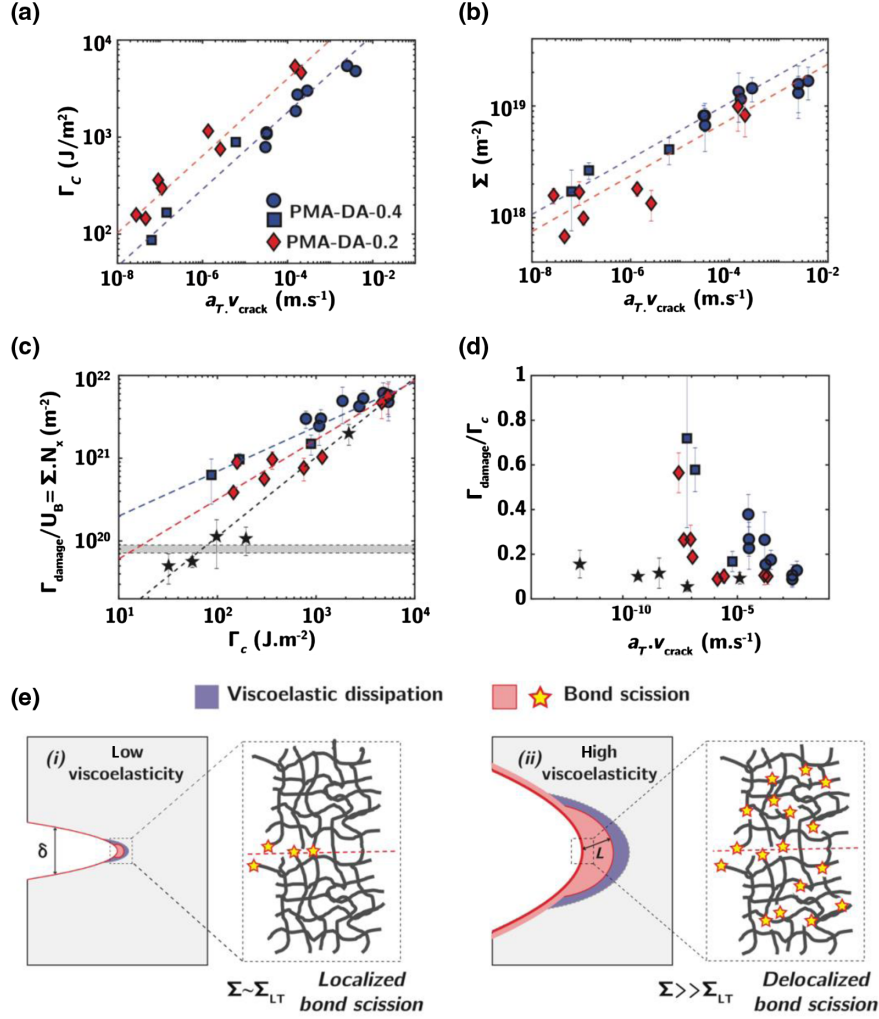
FIG. 5.   Effect of molecular structure and contribution of bond scission to the fracture energy. (a) Fracture energy as a function of the rescaled velocity for two PMA samples with distinct cross-link densities (see Table I). Dashed lines show the power-law fit. (b) Absolute number of cleaved strands per unit area as a function of the rescaled velocities for the two samples. Dashed lines show power-law fits. (c) Rescaled fracture energy due to bond scission $\Gamma_{\text{damage}}/U_B = \Sigma.N_x$ as a function of the total fracture energy Γ_C. Dashed lines are power-law fits with power $\beta = 0.95$, 0.72, and 0.54, respectively for PEA-DA-0.5, PMA-DA-0.4, and PMA-DA-0.2. The gray area represents $(\Gamma_0/U_B) = \Sigma_{\text{LT}}.N_x$, the Lake-Thomas threshold for the three materials. Error bars in (b) and (c) show the standard deviation based on four local confocal measurements on each fractured sample. (d) Ratio $\Gamma_{\text{damage}}/\Gamma_c$ of the energy Γ_{damage} dissipated by bond scission, over the total fracture energy Γ_c, as a function of the reduced crack speed $a_T v_{\text{crack}}$. The energy Γ_{damage} is estimated assuming $U_B = 60$ kJ.mol^{-1}. (e) Schematic coupling between viscoelasticity (blue domain) and strand breakage (red domain) at the crack tip. The enlarged region shows the occurrence of bond scission (yellow stars) in the elastomer network. Bond scission and viscoelastic dissipation are strongly coupled, with a joint increase in bond scission and viscoelastic dissipation between the low viscoelasticity (i) and large viscoelasticity regimes (ii). δ represents the crack tip opening displacement and L the characteristic spatial extension of bond scission at the crack tip.

the energy release rate G, leading to higher strains far from the crack. As discussed in a recent review [9], the elastoadhesive length at propagation Γ_c/E sets the size of the crack tip opening displacement δ and the scale for the onset of nonlinear behaviors at the crack tip. As shown schematically in Fig. 5(e), this increase of $\delta \sim \Gamma_c/E$ with increased crack speed increases all local strains around the crack tip and, hence, the local probability of strand scission. Over the range of stretch rates and temperatures probed

here, the reduced stretch rate is of the order of $a_T \dot{\lambda} \sim 2 \times 10^{-9} - 5 \times 10^{-4}$ s^{-1}, for which the elastic component of the modulus $E' \approx 1$ MPa varies only little with the strain rate (Fig. S7 in Supplemental Material [24]). Given this nearly constant elastic modulus E', the crack tip displacement $\delta \sim \Gamma_c/E'$ should then scale with the reduced crack speed like Γ_c. Since the strain field around the crack tip is directly dependent on δ, the associated areal damage density Σ should increase with δ and, we indeed, observe an

increase in both Γ_c and $\Sigma/\Sigma_{\mathrm{LT}}$ as a function of $a_T.v_{\mathrm{crack}}$ in Figs. 4(a) and 4(b). Note that the saturation of damage for the largest crack velocity could be due to the onset of stiffening of the material (increase in E) for the largest stretch rates (Fig. S7 [24]). In essence, this coupling means that a small increase in viscoelastic dissipation per unit volume far from the tip can cause a commensurable amount of dissipated energy close to the crack tip by bond scission and by the dissipative processes associated with bond scission.

V. EFFECT OF MOLECULAR STRUCTURE

Our methodology allows us to further investigate the effects of the molecular architecture of the material, such as the cross-link density, on bond scission at the crack tip. As shown in Fig. 5(a), when plotting the fracture energy as a function of the rescaled velocity for the two PMA samples with different cross-link densities, we observe that Γ_c is larger for the sample with the lowest cross-link density ν_x [Fig. 5(a), comparing red and blue points] but follows the same power law with $a_T.v_{\mathrm{crack}}$. Intriguingly, as shown in Fig. 5(b), the density Σ of strands cleaved during crack propagation shows a similar scaling; the broken strand density is actually slightly smaller for the PMA-DA-0.2 sample, with the smaller cross-link density and the larger Γ_c [Fig. 5(b), comparing red and blue points].

We can interpret these trends in the molecular framework set by Lake and Thomas [27]. The classical Lake-Thomas model makes two important claims. First, in the absence of viscoelastic dissipation (in threshold conditions), the fracture energy Γ_c is expected to be proportional to the areal density of strands crossing the interface Σ_{LT}. Second, each broken strand dissipates an energy $N_x \cdot U_B$, with N_x the number of backbone bonds in the strand and U_B the rupture energy of a single bond. While these claims are reasonable in threshold conditions (in the absence of viscoelastic dissipation), where they have been checked experimentally [39–41], there are no obvious reasons for the extension of this coupling between strand scission and fracture energy, when additional viscoelastic dissipative processes are at stake in the material. Our measurements nevertheless demonstrate that a network of lower cross-link density leads to more total dissipated energy for fewer broken strands not only in threshold conditions but also for a wider range of crack propagation speeds.

VI. BOND SCISSION AND FRACTURE ENERGY

Since a significant level of bond scission occurs in our material during crack propagation, an important question is the relative contribution of viscoelastic dissipation Γ_{visco} and bond scission Γ_{damage} to the measured fracture energy, expressed as $\Gamma_c = \Gamma_{\mathrm{damage}} + \Gamma_{\mathrm{visco}}$. Extrapolating the argument of Lake and Thomas on strand failure to strands in the bulk, we approximate the energy dissipated per unit area due to bond breakage as $\Gamma_{\mathrm{damage}} = \Sigma \cdot U_{\mathrm{strand}} = \Sigma \cdot N_x \cdot U_B$. The original Lake-Thomas model proposed a value U_B of

350 kJ·mol^{-1} or 3.6 eV for a carbon—carbon bond [27]. A recent analysis of the statistical aspect associated with strand failure based on single molecule stretching experiments provides a more realistic value of 60 kJ·mol^{-1} or 0.6 eV/bond as a sounder estimate [42] for the average energy lost by each C—C bond when the polymer strand breaks. Regardless of the exact value associated with this bond scission energy, we plot in Fig. 5(c) the quantity $\Gamma_{\mathrm{damage}}/U_b = N_x \cdot \Sigma$ (directly proportional to the energy dissipated by bond scission) as a function of the macroscopic fracture energy Γ_c of the material.

Whereas the energy Γ_{damage} dissipated due to bond scission is classically assumed to be constant and proportional to $\Sigma_{\mathrm{LT}}.N_x$ [horizontal gray domain, Fig. 5(c)], we find in Fig. 5(c) a strong correlation between $\Gamma_{\mathrm{damage}}/U_b$ and Γ_c (dashed lines are power-law fits). Bond scission thus contributes to the total fracture energy to a much larger extent than previously thought.

Γ_{damage} can accordingly reach values of 100 times the Lake-Thomas Γ_0 threshold [Fig. 5(c)], i.e., for the PMA-DA-0.4 network, more than 1 kJ/m^2, dissipated over a volume with dimensions of the order of 100 μm near the crack tip. This new experimental insight highlights the so far neglected influence of molecular bond scission at the crack tip on fracture energies and explains why, as already pointed out by Gent [12], purely linear viscoelastic theories typically require viscoelastic dissipation to take place down to unphysically small molecular distances to the crack tip to account for experimentally measured fracture energy.

Our measurements allow us to further compare specifically the behavior of the different networks [Figs. 5(c) and 5(d)]. In Fig. 5(c), we approximate the coupling between bond scission and fracture energies as power laws, with $\Gamma_{\mathrm{damage}} \sim \Gamma_c^{\beta}$ with $\beta = 0.95$, 0.72, and 0.54, respectively, for the three networks. The fraction of energy dissipated through molecular damage and viscoelasticity can be expressed, respectively, as $(\Gamma_{\mathrm{damage}}/\Gamma_c) \sim \Gamma_c^{-(1-\beta)}$ and $(\Gamma_{\mathrm{visco}}/\Gamma_c) \sim (\Gamma_c - \Gamma_{\mathrm{damage}}/\Gamma_c) \sim 1 - \Gamma_c^{-(1-\beta)}$. The scaling coefficient $\beta \lesssim 1$ for all three networks suggests a slow and progressive transition from a strand scission-dominated regime to a viscoelasticity-dominated regime, without any simple decoupling between Γ_{damage} and Γ_{visco}. Figure 5(d) additionally shows the ratio $\Gamma_{\mathrm{damage}}/\Gamma_c$ as a function of $a_T V$ (taking the value $U_B = 60$ kJ.mol^{-1} for the bond breakage energy). Interestingly, this ratio varies from 0.8 to 0.2 as $a_T V$ increases, and, while the trend is clear, the relative importance of chain scission and viscoelastic dissipation does seem to depend both on the cross-linking ratio and on the nature of the polymer itself.

In summary, and as schematically represented in Fig. 5(e), increasing the crack speed and increasing viscoelasticity (blue domain) lead to an increase in crack opening and, as a result, to a delocalization of damage and

to an increase in the energy dissipated by strand scission (red domain).

VII. CONCLUSION

The labeling of elastomeric networks with fluorogenic mechanophores that become fluorescent upon scission gives unprecedented insights in the bond scission processes occurring at the crack tip as the material breaks. Our measurements unveil that, contrary to previous belief, bond scission in these simple networks can extend over more than 100 μm from the crack plane and is strongly dependent on the bulk viscoelastic properties of the network. These observations contradict classical models assuming spatial decoupling between strain-rate-independent damage processes at the crack tip and bulk viscoelastic dissipation. These new experimental insights suggest, instead, the occurrence of intrinsically coupled processes between strand scission and viscoelastic relaxation, mediated by an increase in local strains at the crack tip. Bond scission accordingly accounts for a much larger amount of the fracture energy than anticipated, especially in conditions of large viscoelasticity, and is an overlooked key factor to understand and model fracture toughness from molecular structure.

Our methodology and measurements on model networks open far-reaching and diverse paths. It can be used to quantitatively reevaluate a number of damage processes as, e.g., occurring during soft material long-term failure and reveal previously invisible damage in a nondestructive way. Our study should further guide the engineering and control of dissipative bond scission processes in complex tough soft materials such as engineering elastomers or tough hydrogels and stimulate the development of new multiscale models and simulations of elastomer fracture, coupling bond scission and viscoelastic behavior.

All data needed to evaluate the conclusions in the paper are present in the paper and/or Supplemental Material [24]. Additional data available from authors upon request.

APPENDIX A: MATERIAL SYNTHESIS

1. Materials and methods

Reagents were purchased from commercial suppliers (TCI Chemicals, VWR, Sigma-Aldrich) and used as received. NMR spectra are recorded on a 400 MHz (100 MHz for ^{13}C) Varian Mercury VX spectrometer at room temperature using residual protonated solvent signals as internal standards [^{1}H: δ(CDCl$_3$) = 7.26 ppm; ^{13}C: δ(CDCl$_3$) = 77.16 ppm].

Purity and exact mass of the synthesized compounds are determined using an LCQ Fleet (Thermo Finnigan) ion-trap mass spectrometer equipped with a Surveyor autosampler and Surveyor PDA detector (Thermo Finnigan). Solvents are pumped with a flow of 0.2 mL·min^{-1} using a high-pressure gradient system using two LC-10AD pumps (Shimadzu). Before mass analysis, the crude is run over a reverse phase C$_{18}$ column (GraceSmart 2×50 mm, Grace) using a 2%–90% MeCN linear gradient in H$_2$O with 0.1% formic acid.

2. Diels-Alder adduct mechanophore synthesis

The synthetic procedure of the Diels-Alder adduct mechanophore is adapted from the procedure developed by the groups of Göstl and Sijbesma [18,23]. The five-step synthesis is described in Supplemental Material [24], Sec. S1 and Figs. S1–S4. The final product is noted DACL (for Diels-Alder adduct cross-linker). Intermediate species are noted DACL1–4.

3. Network synthesis

Samples are prepared through photoinduced free radical polymerization following a previously published general procedure [19,21]. 2-Hydroxy-2-methylpropiophenone (HMP) is used as an UV initiator. The standard cross-linker used is 1,4-butanediol diacrylate (BDA). Monomer, cross-linker, and initiator (1.16 mol% relative to monomer) are mixed, and the solution is cast in a mold. The latter is composed of two glass plates covered with transparent PET films (with a hydrophobic surface), with a silicone spacer

TABLE II. Composition of the various materials in mol% with respect to monomer concentration.

	HMP (mol%)	Total cross-linker (mol%)	BDA (mol%)	DACL (mol%)
PMA-DA-0.4	1.16	0.43	0.41	0.02
PMA-04	1.16	0.43	0.43	0
PMA-DA-0.2	1.16	0.22	0.2	0.02
PEA-DA-0.5	1.16	0.5	0.48	0.02

to control the sample thickness (0.7 mm) and two metal frames to seal the mold. The mold is placed under UV ($\lambda = 365$ nm) for 2 h. The UV power is kept low (below $10~\mu\text{W cm}^{-2}$) to induce a slow polymerization in order to decrease the number of simultaneous growing chains and the number of termination reactions.

After polymerization, the sample was dried overnight *in vacuo* (without heating) to remove unreacted volatile monomer. The sample is weighed before and after drying. The weight loss is less than 0.2%.

The cross-linker concentration is adjusted to tune the properties of the various materials (see Table II). For each material, up to three samples are obtained from one polymerization batch. For each polymerization, run on the same day, the reactive medium is taken from the same stock solution (monomer, cross-linkers), and the initiator is added prior to each polymerization.

4. Incorporation of the mechanophore into the network

To label the samples with mechanophores, the Diels-Alder adduct mechanophore diacrylate cross-linker (DACL) is covalently incorporated. The DACL is used in combination with the mechanochemically nonresponsive cross-linker BDA. The mechanophore cross-linker is introduced at a concentration of 0.02 mol%. This small quantity is sufficient for damage detection by fluorescence.

APPENDIX B: NETWORK PROPERTIES AND CHARACTERIZATION

The glass transition temperature T_g of PMA and PEA networks is measured from dynamic mechanical analysis, based on an estimation of the inflection point of the storage modulus. We find T_g of $-18\,°\text{C}$ and $18\,°\text{C}$ for the PMA and PEA networks, respectively.

1. Evaluation of network cross-link density for the Lake-Thomas model

To properly characterize the density of cross-links and entanglements in our materials, we fit the stress-strain curve of the notched samples, with the network elasticity model proposed by Rubinstein and Panyukov [43]. Stress-strain curves are corrected for notch opening. We use

TABLE III. Parameters used for the estimation of areal chain density. Values of C_∞ and ρ are from Ref. [44].

	l_0 (nm)	C_∞	ρ (kg.m^{-3})	M_0 (g.mol^{-1})
MA	0.154	8.1	1220	86.09
EA	0.154	9.3	1120	100.12

measurements at $\dot{\lambda} = 3.10^{-3}~\text{s}^{-1}$ and $T = -5\,°\text{C}$ and $T = 25\,°\text{C}$ for the PEA and PMA samples, respectively, allowing us to fit the stress-strain curves up to $\lambda = 2.6$. This fit allows us to extract the contribution of cross-links E_x and entanglements E_e, from

$$\sigma = \frac{1}{3}\left(\lambda - \frac{1}{\lambda^2}\right)\left(E_x + \frac{E_e}{0.74\lambda + 0.61\lambda^{-0.5} - 0.35}\right).$$

The average number N_x of monomer between cross-links is then estimated from E_x as

$$N_x = \frac{6\rho RT}{M_{\text{monomer}} E_x}.$$

We find $E_x = [0.6; 0.35; 0.5]$ and $E_e = [0.7; 0.7; 0.5]$ for, respectively, PMA-DA-0.4 at 25 °C, PMA-DA-0.2 at 25 °C, and PEA-DA-0.5 at −5 °C (values are averaged over two samples for PMA). As expected, the contribution of entanglements E_e is the same for the two PMA samples. The fact that the ratio between cross-link contribution E_x is not exactly two between PMA-DA-0.4 and PMA-DA-0.2 is probably due to the difference in reactivity between monomer and cross-linker leading to a different efficiency in the incorporation of the cross-linker in the network.

2. Lake-Thomas chain density

From Gaussian statistics, we can express Σ_{LT}, the areal density of polymer strand crossing an arbitrary plane, as [37]

$$\Sigma_{\text{LT}} = 1/2 \cdot v_x \langle R_0^2 \rangle^{1/2} = \frac{l_0 E_x \sqrt{C_\infty N_x}}{6 k_B T} = l_0 \left(\frac{E_x \rho N_A C_\infty}{6 M_0 k_B T}\right)^{1/2}$$

with ν_x the bulk density of cross-linking points, $\langle R_0^2 \rangle^{1/2}$ the average distance between cross-links, l_0 the length of a C—C bond, E_x the modulus due to cross-linking, ρ the density of the monomer, M_0 the molar mass of the monomer, T the temperature, and k_B the Boltzmann constant. The parameters used for EA and MA network are reported in Table III.

APPENDIX C: DAMAGE QUANTIFICATION

1. Confocal setup

Confocal images on PMA-DA-0.4 and PMA-DA-0.2 samples are taken with a customized Nikon AZ-100/C2+ confocal macroscope. The objective used is an AZ Plan Fluor 5×, with a focal length of 15 mm. The objective is upright and can zoom from 1× to 8×, with the use of the

$5\times$ zoom for quantitative image analysis. Pixel size is 1.63 μm. Image size is 835×835 μm (512×512 px).

Confocal images of the PEA-DA-0.5 sample are taken with a Leica TCS SP8 CSU. We use an inverted $63\times$ oil immersion objective (NA 1.4). Pixel size is 180 nm. Image size is 184.7×184.7 μm (1024×1024 px).

We use an excitation wavelength $\lambda = 405$ nm and recorded emission from 450 to 550 nm.

2. Confocal image collection

Crack propagation occurs throughout most of our experiments in a well-defined plane. In cases where few crack bifurcations appear (e.g., PEA at 40 °C and 60 °C), we restrict our image analysis to the regions of planar cracks. In all samples, the signal is homogenous throughout the thickness, and the 3D nature of the process can, thus, be simplified to a 2D analysis.

For systematic analysis, single optical sections are recorded in the area where the crack propagates. The images are taken perpendicular to the crack surface. Samples are immersed in glycerol to avoid refractive index mismatch at the crack surface (refractive index of PEA, PMA [45], and glycerol are, respectively, 1.464, 1.479, and 1.4722). The top of the sample is identified as the plane of maximal intensity. The focal plane is then displaced at 100 μm depth from the top of the sample for all quantification. Laser and gain are adapted for each set of experiments.

The sample is broken in two pieces following the crack propagation test. Two images at the beginning and end of the crack length are recorded for each side (four pictures per sample). Error bars in the main text [Figs. 4(b), 4(c), and 5(a)–5(c)] characterize standard deviation due to this spatial variability.

3. Vignetting and flat-field correction

During imaging with the AZ-100/C2+ confocal macroscope, the low magnification of the optical system results in vignetting (inhomogeneous illumination and gradual intensity darkening toward the corners). To correct for vignetting, we measure the intensity $I_{\text{FlatField}}$ in a calibration sample with a homogeneous concentration of fluorescent calibration molecule. The corrected image of the crack surface I_{corr} is taken as $I_{\text{corr}} = I_{\text{original}}/I_{\text{FlatField}}$. We furthermore restrict all quantitative analysis of damage to a distance of 500 μm along the crack profile (see main text, Fig. 3).

4. Calibration of fluorescence intensity

To convert fluorescence intensity to a concentration of activated molecules, we use calibration samples. The calibration molecule [9-((4-anisyl)ethynyl)anthracene] [18] is solution blended directly with linear PEA chains ($M_w \sim 95$ kg·mol^{-1} in toluene from Sigma-Aldrich). The
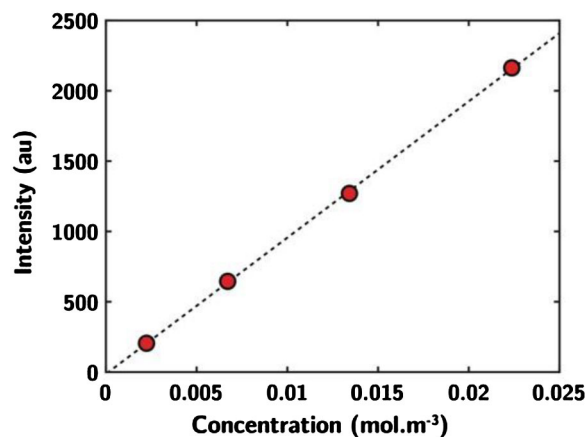

FIG. 6. Calibration of fluorescence intensity with mechanophore concentration. Typical calibration curve, showing the linear relation between fluorescence intensity and concentration of calibration molecule.

solvent is evaporated under a fume hood for one day and *in vacuo* overnight, leading to calibration samples with a homogeneous and known concentration of fluorescent molecules.

As fluorescence originates from the π-extended anthracene moiety, which is present both in the calibration molecule and in the activated mechanophore and because the environment is similar (PEA chains), the calibration molecule is assumed to have the same fluorescence properties as the activated mechanophore. Phase separation is not present at the optical scale, as verified by confocal fluorescence microscopy. The concentration of activated mechanophores can, thus, be measured based on the intensity of the calibration molecule. By varying the concentration of the calibration molecule, a calibration curve of fluorescence intensity vs activated mechanophore concentration (mol · m^{-3}) is constructed as shown in Fig. 6.
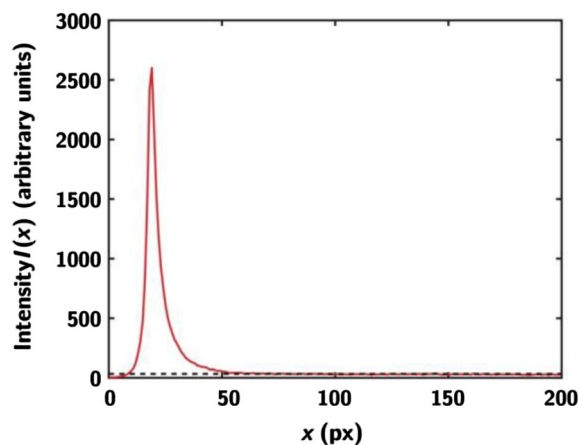

FIG. 7. Damage profile extraction. Intensity normal to the crack profile. The horizontal dashed line shows the background level in the material.

This calibration procedure is repeated each time a new set of optical measurements is taken.

5. Quantitative image analysis

We measure the intensity profile $I(x)$ perpendicular to the crack edge and define the background intensity I_{bkg} (Fig. 7). The concentration profile $c(x)$ [and the fraction of activated mechanophore $\phi(x)$] is calculated as $c(x) = \alpha[I(x) - I_{bkg}]$ with α the coefficient obtained from the calibration curve (Fig. 6).

6. Representativity of mechanophore activation for chain damage

To verify that mechanophore activation and fluorescence intensity are indeed representative of chain scission, we synthetize four samples with different concentrations of DACL while keeping the overall cross-linker concentration constant (0.41 mol%, corresponding to PMA-DA-04, Table II). We propagate cracks at a stretch rate of $\dot\lambda = 3 \times 10^{-3}$ s^{-1} in these samples and quantify the fraction of activated mechanophore per unit area of crack. As shown in Fig. 8(a), we observe a nearly linear relation between activated mechanophore concentration and the molar

fraction of mechanophore in the first network, indicating that the activation of mechanophores in the network is indeed representative of chain scission. Additionally, Fig. 8(b) shows that the damage profiles for the four different DACL concentration are indeed independent of the initial molar fraction of mechanophore incorporated in the network. In terms of mechanical properties, replacing $\phi = 5\%$ of the cross-linkers by a weaker mechanophore cross-linker is in the worst case equivalent to diluting the effective number of mechanically active chains per volume by ϕ (assuming the mechanophore link as infinitely weak), leading to $\nu_x^{\text{eff}} = (1 - \phi)\nu_x^0$. The areal density of nonmechanophore chains can then be expressed as $\Sigma \sim (\nu_x^{\text{eff}})^{2/3} \sim (1 - \phi)^{2/3}\Sigma_0$. Expressing the fracture energy as $\Gamma = N_x \Sigma U$, it has then only a weak scaling with ϕ (a 10% change in ϕ leads to a 7% change in fracture energy assuming that N does not change) that is within experimental error.

7. Intrinsic activation of mechanophore as a function of stretch rate and temperature

Mechanophore activation via the retro Diels-Alder reaction (see Fig. 2) could be intrinsically biased by the temperature or strain rate. To probe this effect, we
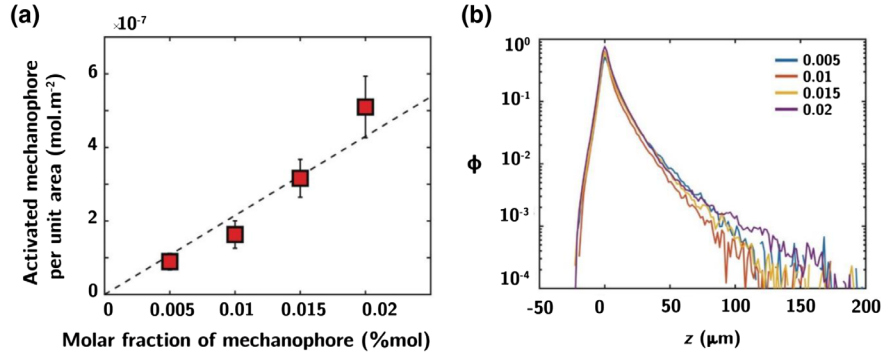

FIG. 8. Linear dependence of fluorescence intensity with mechanophore concentration. (a) Linear dependence of activated mechanophore per unit area as a function of the molar fraction of mechanophore. (b) Absolute damage profiles $\phi(z)$ for various molar fractions of mechanophore.
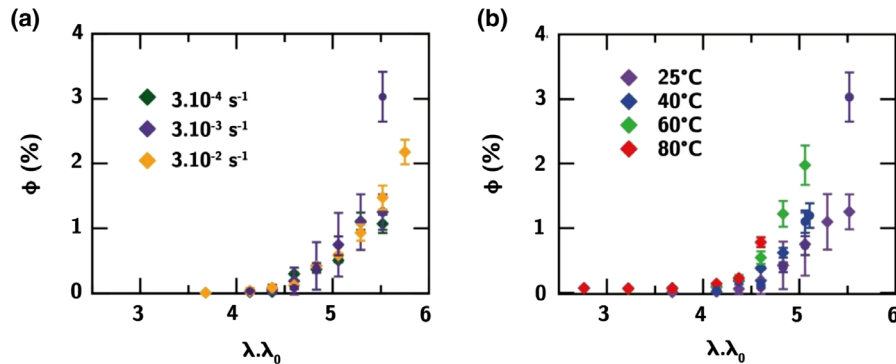

FIG. 9. Intrinsic activation of mechanophore as a function of the stretch rate and temperature. Bulk fraction of activated mechanophore in the triple network, as a function of the stretch $\lambda \cdot \lambda_0$ on the first network for (a) various stretch rates and (b) temperatures.

synthetize a multiple network elastomer network of PMA as previously described in detail [19,21,37] with the first network containing the DACL mechanophore. This multiple network structure (obtained by swelling and polymerization steps) leads to an isotropic prestretch $\lambda_0 = 2.3$ of the network synthesized first and allows us to apply large strains to this mechanophore-labeled network without macroscopically breaking the material. We can thus probe the intrinsic activation of the mechanophore under various conditions of strain and temperature. As shown in Fig. 9, we stretch this sample to various λ, leading to a stretch $\lambda \cdot \lambda_0$ on the first network, and measure the bulk activation ϕ of the mechanophore. As reported in Fig. 9(a), within our experimental reproducibility, bulk mechanophore activation appears independent of the strain rate. We measure a slight increase in mechanophore activation at higher temperatures [Fig. 9(b)], which could be an indication of thermally biased scission of the DACL bond. This effect could lead to the overestimation of damage at a large temperature. However, as shown in Figs. 4 and 5, we observe a large decrease in mechanophore activation at the fracture surface for an increasing temperature. Such a slight damage overestimation at a larger temperature does not affect our conclusion.

---

[1] J. P. Gong, Y. Katsuyama, T. Kurokawa, and Y. Osada, *Double-Network Hydrogels with Extremely High Mechanical Strength*, Adv. Mater. **15**, 1155 (2003).

[2] T. Matsuda, R. Kawakami, R. Namba, T. Nakajima, and J. P. Gong, *Mechanoresponsive Self-Growing Hydrogels Inspired by Muscle Training*, Science **363**, 504 (2019).

[3] J.-Y. Sun, X. Zhao, W. R. K. Illeperuma, O. Chaudhuri, K. H. Oh, D. J. Mooney, J. J. Vlassak, and Z. Suo, *Highly Stretchable and Tough Hydrogels*, Nature (London) **489**, 133 (2012).

[4] E. Filippidi, T. R. Cristiani, C. D. Eisenbach, J. Herbert Waite, J. N. Israelachvili, B. K. Ahn, and M. T. Valentine, *Toughening Elastomers Using Mussel-Inspired Iron-Catechol Complexes*, Science **358**, 502 (2017).

[5] I. R. Minev *et al.*, *Electronic Dura Mater for Long-Term Multimodal Neural Interfaces*, Science **347**, 159 (2015).

[6] C. Keplinger, J.-Y. Sun, C. C. Foo, P. Rothemund, G. M. Whitesides, and Z. Suo, *Stretchable, Transparent, Ionic Conductors*, Science **341**, 984 (2013).

[7] H. Yuk, S. Lin, C. Ma, M. Takaffoli, N. X. Fang, and X. Zhao, *Hydraulic Hydrogel Actuators and Robots Optically and Sonically Camouflaged in Water*, Nat. Commun. **8**, 14230 (2017).

[8] B. N. J. Persson, O. Albohr, G. Heinrich, and H. Ueba, *Crack Propagation in Rubber-like Materials*, J. Phys. Condens. Matter **17**, R1071 (2005).

[9] C. Creton and M. Ciccotti, *Fracture and Adhesion of Soft Materials: A Review*, Rep. Prog. Phys. **79**, 046601 (2016).

[10] R. Bai, J. Yang, and Z. Suo, *Fatigue of Hydrogels*, Eur. J. Mech. A **74**, 337 (2019).

[11] B. N. J. Persson and E. A. Brener, *Crack Propagation in Viscoelastic Solids*, Phys. Rev. E **71**, 036123 (2005).

[12] A. N. Gent, *Adhesion and Strength of Viscoelastic Solids. Is There a Relationship between Adhesion and Bulk Properties?*, Langmuir **12**, 4492 (1996).

[13] R. Long and C.-Y. Hui, *Fracture Toughness of Hydrogels: Measurement and Interpretation*, Soft Matter **12**, 8069 (2016).

[14] R. A. Schapery, *Theory of Crack Initiation and Growth in Viscoelastic Media. 2. Approximate Methods of Analysis*, Int. J. Fract. **11**, 369 (1975).

[15] W. G. Knauss, in *Deformation, and Fracture of High Polymers*, edited by H. H. Kausch, J. A. Hassell, and R. I. Jaffee (Springer, New York, 1973), p. 501.

[16] D. A. Davis *et al.*, *Force-Induced Activation of Covalent Bonds in Mechanoresponsive Polymeric Materials*, Nature (London) **459**, 68 (2009).

[17] Y. Chen, A. J. H. Spiering, S. Karthikeyan, G. W. M. Peters, E. W. Meijer, and R. P. Sijbesma, *Mechanically Induced Chemiluminescence from Polymers Incorporating a 1,2-Dioxetane Unit in the Main Chain*, Nat. Chem. **4**, 559 (2012).

[18] R. Gostl and R. P. Sijbesma, *[small pi]-Extended Anthracenes as Sensitive Probes for Mechanical Stress*, Chem. Sci. **7**, 370 (2016).

[19] E. Ducrot, Y. Chen, M. Bulters, R. P. Sijbesma, and C. Creton, *Toughening Elastomers with Sacrificial Bonds and Watching Them Break*, Science **344**, 186 (2014).

[20] J. M. Clough, C. Creton, S. L. Craig, and R. P. Sijbesma, *Covalent Bond Scission in the Mullins Effect of a Filled Elastomer: Real-Time Visualization with Mechanoluminescence*, Adv. Funct. Mater. **26**, 9063 (2016).

[21] Y. Chen, C. J. Yeh, Y. Qi, R. Long, and C. Creton, *From Force Responsive Molecules to Quantifying and Mapping Stresses in Soft Materials*, Sci. Adv. **6**, eaaz5093 (2020).

[22] J. P. Gong, *Why Are Double Network Hydrogels So Tough?*, Soft Matter **6**, 2583 (2010).

[23] D. Yildiz, C. Baumann, A. Mikosch, A. J. C. Kuehne, A. Herrmann, and R. Göstl, *Anti-Stokes Stress Sensing: Mechanochemical Activation of Triplet-Triplet Annihilation Photon Upconversion*, Angew. Chem., Int. Ed. **58**, 12919 (2019).

[24] See Supplemental Material at http://link.aps.org/supplemental/10.1103/PhysRevX.10.041045 for material synthesis, Mechanical measurements and network properties and characterization.

[25] H. W. Greensmith, *Rupture of Rubber. X. The Change in Stored Energy on Making a Small Cut in a Test Piece Held in Simple Extension*, J. Appl. Polym. Sci. **7**, 993 (1963).

[26] T. L. Smith, *Ultimate Tensile Properties of Elastomers. I. Characterization by a Time and Temperature Independent Failure Envelope*, J. Polym. Sci., Part A: Gen. Pap. **1**, 3597 (1963).

[27] G. J. Lake and A. G. Thomas, *The Strength of Highly Elastic Materials*, Proc. R. Soc. A **300**, 108 (1967).

[28] P. G. de Gennes, *Soft Adhesives*, Langmuir **12**, 4497 (1996).

[29] N. Sakumichi and K. Okumura, *Exactly Solvable Model for a Velocity Jump Observed in Crack Propagation in Viscoelastic Solids*, Sci. Rep. **7**, 8065 (2017).

[30] K. Grosch, J. A. C. Harwood, and A. R. Payne, *Breaking Energy of Rubbers*, Nature (London) **212**, 497 (1966).

[31] W. G. Knauss, *A Review of Fracture in Viscoelastic Materials*, Int. J. Fract. **196**, 99 (2015).

[32] R. Long, C. Y. Hui, J. P. Gong, and E. Bouchbinder, *The Fracture of Highly Deformable Soft Materials: A Tale of Two Length Scales*, arXiv:2004.03159.

[33] S. Akbulatov and R. Boulatov, *Experimental Polymer Mechanochemistry and Its Interpretational Frameworks*, ChemPhysChem **18**, 1422 (2017).

[34] E. Izak-Nau, D. Campagna, C. Baumann, and R. Göstl, *Polymer Mechanochemistry-Enabled Pericyclic Reactions*, Polym. Chem. **11**, 2274 (2020).

[35] F. J. Vernerey, R. Brighenti, R. Long, and T. Shen, *Statistical Damage Mechanics of Polymer Networks*, Macromolecules **51**, 6609 (2018).

[36] Y. Mao, B. Talamini, and L. Anand, *Rupture of Polymers by Chain Scission*, Extreme Mech. Lett. **13**, 17 (2017).

[37] P. Millereau, E. Ducrot, J. M. Clough, M. E. Wiseman, H. R. Brown, R. P. Sijbesma, and C. Creton, *Mechanics of Elastomeric Molecular Composites*, Proc. Natl. Acad. Sci. U.S.A. **115**, 9110 (2018).

[38] P. G. de Gennes, *Fracture d'un Adhésif Faiblement Réticulé*, C. R. Acad. Sci. Paris, Ser. II **307**, 1949 (1988).

[39] A. Ahagon and A. N. Gent, *Threshold Fracture Energies for Elastomers*, J. Polym. Sci., Polym. Phys. Ed. **13**, 1903 (1975).

[40] A. N. Gent and R. H. Tobias, *Threshold Tear Strength of Elastomers*, J. Polym. Sci., Polym. Phys. Ed. **20**, 2051 (1982).

[41] Y. Akagi, H. Sakurai, J. P. Gong, U.-i. Chung, and T. Sakai, *Fracture Energy of Polymer Gels with Controlled Network Structures*, J. Chem. Phys. **139**, 144905 (2013).

[42] S. Wang, S. Panyukov, M. Rubinstein, and S. L. Craig, *Quantitative Adjustment to the Molecular Energy Parameter in the Lake–Thomas Theory of Polymer Fracture Energy*, Macromolecules **52**, 2772 (2019).

[43] M. Rubinstein and S. Panyukov, *Elasticity of Polymer Networks*, Macromolecules **35**, 6670 (2002).

[44] J. E. Mark, *Physical Properties of Polymers* (American Institute of Physics, Woodbury, NY, 1996), p. 723.

[45] J. E. Mark, *Polymer Data Handbook* (Oxford University Press, New York, 2009), Vol. 1, p. 1250.